



Study on the influence of fracture dip angle on mechanical and acoustic emission characteristics of deep granite

Xiqi Liu^{1,2} · Gang Wang^{1,2} · Leibo Song² · Rong Hu³ · Xiaoming Ma⁴ · Xiaoping Ou⁵ · Shiji Zhong⁵

Received: 15 January 2023 / Accepted: 26 April 2023 / Published online: 6 May 2023
© The Author(s), under exclusive licence to Springer Nature B.V. 2023

Abstract

To study the influence of fracture dip angle on the mechanical properties and fracture evolution mechanism of granite under triaxial stress state, MTS 815 mechanics test system was used to conduct triaxial tests on granite with different fracture dip angles, and PCI-II acoustic emission (AE) system was used to monitor the whole process information. The results show that the brittle characteristics of fractured samples with 30°, 45° and 60° dip angles are obviously weakened, while the plastic characteristics are enhanced. The fractures destroy the structural integrity of rock, resulting in the reduction of rock resistance to load and deformation. With the increase in fracture dip angles from 0° to 90°, the compressive strength and elastic modulus of rock samples show a nearly "U"-shaped changing trend of decreasing first and then increasing, and the deterioration ratio coefficients are 7.8~43.3% and 7.5~66.9%, respectively. Due to the difference of fracture dip angles, the failure of granite sample shows two modes: "through-cutting fracture surface failure" and "shear failure along fracture surface." It mainly depends on the angle between fracture surface and maximum principal stress. The fracture dip angle affects the variation law of AE signals during the fracture process. Especially for the fractured rock samples with 30°, 45° and 60° dip angles, the AE ring count and energy show obvious "migration" phenomenon, and the signal concentration distribution area is widened and moved backward. With the increase in dip angle, the active degree of rock fracture decreases at first and then increases.

Keywords Rock mechanics · Fracture dip angle · Triaxial compression · Mechanical properties · Acoustic emission characteristics

✉ Gang Wang
gangw277842@whut.edu.cn

¹ Key Laboratory of Geotechnical and Structural Engineering Safety of Hubei Province, School of Civil Engineering, Wuhan University, Wuhan 430070, China

² Collaborative Innovation Center for Prevention and Control of Mountain Geological Hazards of Zhejiang Province, Shaoxing University, Shaoxing 312099, China

³ School of Civil Engineering, University of South China, Hengyang 421001, China

⁴ Huahui Engineering Design Group Co., Ltd., Shaoxing 312000, China

⁵ China Gezhouba Group No. 1 Engineering Co., Ltd., Yichang 443000, China

1 Introduction

Rock mass, as a complex engineering medium, will produce many different kinds of defects, such as cracks, weak surfaces and faults, under the complex and long geological processes (Rudziński et al. 2019; Liu et al. 2020; Song et al. 2022a). In deep rock mass engineering, the existence of these defects makes the rock mass show obvious heterogeneity, discontinuity, anisotropy and other characteristics, which has a significant impact on the strength properties, deformation characteristics and stability of the rock mass (Mohammadi and Pietruszczak 2019; Latyshev and Prishchepa 2020; Shahbazi et al. 2021). Therefore, the mechanics, deformation characteristics and failure mechanism of rock mass with defects have always been the hot issues concerned by numerous scholars.

Because model test and numerical simulation methods are relatively easy to implement for single crack or multi-cracks rock samples, these two types of test methods are used by many scholars at home and abroad to analyze the influence of fractures on rock mechanical properties. Duan et al. (2019) prepared six samples with three different connectivity and two fracture dip angles using rock-like materials. Through triaxial loading test, it is found that with the increase in fracture angle, fracture connectivity and confining pressure, the transformation of sample from mixed failure to shear failure is accelerated. Lee and Jeon (2011) analyzed the propagation law of fracture under uniaxial compression based on discrete element numerical method. Yu et al. (2020) carried out PFC^{2D} particle flow simulation tests of single fractured sandstone under different confining pressures. The results showed that the influence of fracture dip angle on the peak strength of the sample showed a changing trend of decreasing first and then increasing, and the macro-cracks mainly penetrated from the tip of the prefabricated fracture to the two diagonal points of the sample. Zuo et al. (2013) conducted uniaxial and triaxial compression tests using the FLAC3D finite difference program to study the strength and deformation characteristics of layered rock mass. Li et al. (2015) used the numerical simulation software UDEC to simulate the rock mass with different dip angles of fracture surfaces when the confining pressure is constant and studied the evolution of the compressive strength of single fracture rock with the dip angles of fracture surfaces. It was found that the fracture dip angle has a significant effect on the compressive strength of rock mass, and the compressive strength reaches the lowest value when the dip angle is between 45° and 60°. Huang et al. (2016) analyzed the strength characteristics and deformation characteristics of rock-like materials with intact and discontinuous non-parallel double fractures through the composite model samples of prefabricated cracks. The test showed that the peak strength, crack damage threshold and peak strain of intact and discontinuous fractured rock samples increased linearly with the increase in confining pressure. The research results (Table 1) have laid a foundation for revealing the rock fracture behavior under triaxial compression. However, most of them still assume that the numerical model belongs to plane stress or plane strain problem, and there is a big gap between the rock-like material and the real fractured rock sample. Therefore, it will cause the complex and uncertain mechanical properties of fracture rock mass (Huang et al. 2002; Li et al. 2005; Yang et al. 2007).

In this study, based on MTS electro-hydraulic servo loading system, triaxial loading tests are carried out on fractured granite samples, and acoustic emission system is used to monitor the test process in real time. According to the test results, the influence law of fracture dip angle on rock strength characteristics and deformation characteristics is

Table 1 Statistical table of peer's results

Category	Research method	Factor	Researchers
Numerical simulation methods	Particle flow code	Fracture dip; confining pressure	Yu et al. (2020); Huang et al.(2016); Lee and Jeon (2011)
	Finite difference program	Fracture dip	Zuo et al.(2013)
	Universal distinct element code	Fracture dip	Li et al. (2015)
Model test	Rock-like materials	Connectivity; fracture dip; confining pressure	Duan et al. (2019); Huang et al.(2016)

analyzed, and the acoustic emission characteristics and failure mechanism of fractured granite under triaxial compression are deeply explored. It provides a certain reference for the selection of design parameters and stability control of deep fracture rock mass engineering.

2 Experimental method

2.1 Sample preparation

The rock used in the test is fine-medium-grained monzogranite, as shown in Fig. 1. The mineral composition of the sample analyzed by X-ray diffraction mainly includes quartz (44%), K-feldspar (32%) and albite (20%), and the accessory minerals are biotite (about 3%) and muscovite (about 1%), with a particle size of 2–5 mm. At the same time, the granite contains trace magnetite, apatite, sphene and other heavy mineral components. The granite has a massive structure, with silvery white color and dark spots. It is observed by scanning electron microscope that the granite has a high degree of recrystallization, fine and uniform rock grains, compact structure, intact and compact rock, and few primary cracks. The longitudinal wave velocity of granite rock samples is 4374~4667 m/s after being tested by wave velocity tester. These rock samples have similar integrity.

The rock samples are processed in the same direction to ensure that there is no obvious macroscopic difference between the test rock samples. According to the requirements of the International Society of Rock Mechanics (ISRM) (Luo et al. 2022), the rock sample is processed into a standard cylindrical sample of $\Phi 50 \times 100$ mm. The fracture of rock sample is prepared by wire cutting processing method. A prefabricated fracture of 25 mm in length and 0.4 mm in width is made at the geometric center of the sample, and the fracture dip angle is θ . (θ is the angle between the fracture surface and the maximum principal stress.) The hole with a diameter of 2 mm is unavoidable in the process of crack making, and it does not affect the subsequent experimental study. In order to study the influence law of fracture dip angle θ on the deformation and strength characteristics of rock samples under high confining pressure, five groups of samples with fracture dip angles θ of 0° , 30° , 45° , 60° and 90° are selected, and the prepared fractured rock samples made are shown in Fig. 2.

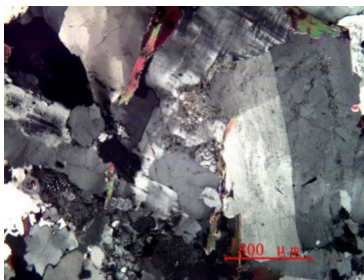
2.2 Test loading scheme

MTS electro-hydraulic servo rock mechanics test system and PAC full information acoustic emission signal analyzer (Fig. 3) are adopted. In the test, the axial deformation and circumferential deformation of the sample are measured by displacement sensor, and the circumferential deformation is measured by chain circumferential displacement sensor. Six acoustic emission sensor probes are symmetrically arranged on the outer surface of the rock. The probe model is RS-2A, the size is $\Phi 12 \times 6$ mm, the acquisition frequency range is 50–400 kHz, the center frequency is 150 kHz, and the applicable temperature is $-20 \sim 130$ °C. The contact part between the sensor and the rock sealing sleeve is coated with Vaseline to ensure the coupling effect and is fixed with adhesive tape. Through AE time sequence characteristics and positioning information, the generation and development of micro-cracks in the process of rock fracture are monitored. The loading process is as follows.

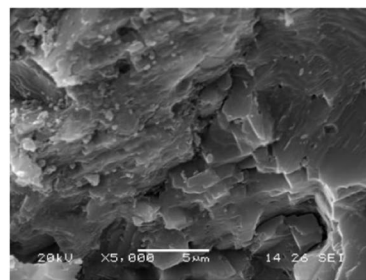
- (1) According to the hydrostatic pressure condition $\sigma_1 = \sigma_2 = \sigma_3$, the confining pressure is applied to the predetermined value of 40 MPa at the loading rate of 0.5 MPa/s, and then, the parameters such as displacement are cleared.
- (2) The confining pressure is kept constant, and the axial load is controlled by displacement. The loading speed of 0.05 mm/min is loaded on the sample to the peak value, and the test is finished until the sample has a large residual deformation. In order to understand the internal mechanism and evolution law of rock failure, acoustic emission system is used to monitor the whole process of granite loading failure. The sampling frequency is 10 MHz, the preamplifier gain is 30 dB, and the noise threshold is 40 dB to minimize noise interference.

2.3 AE positioning technology

In order to clarify the damage and failure evolution process of granite, the location technology based on Geiger algorithm (Zhao et al. 2008) is used for AE event tracking. By obtaining the time difference between different probes when the same AE event occurs,



(a) Microelectron structure of granite by polarizing microscope



(b) Micrograph by scanning electron microscope

Fig. 1 Microscopic structure of granite. **a** Microelectron structure of granite by polarizing microscope and **b** Micrograph by scanning electron microscope



Fig. 2 Granite sample with pre-existing cracks

the spatial location of the AE event can be obtained more accurately (Niu et al. 2023). The specific principle is described as follows:

Multiple iterations are performed based on the set initial point $\theta(x, y, z, t)$ (test point). During each iteration, a correction vector $\Delta\theta(\Delta x, \Delta y, \Delta z, \Delta t)$ can be obtained by using the least square method and added to the results (test points) of the previous iteration. Then, a new test point can be obtained. After that, it can be judged whether the new test point meets the error requirements of the location of the real fracture source. If the error requirements are met, the iteration is terminated. Each iteration result can be obtained through the relationship between time and distance, which can be expressed as:

$$\left[(x_i - x)^2 + (y_i - y)^2 + (z_i - z)^2 \right]^{\frac{1}{2}} = v_p(t_i - t) \tag{1}$$

where x, y and z are the initial coordinates of the test point, t is the initial time of the AE event, x_i, y_i and z_i are the spatial position of the i th AE probe, t_i is the actual time of the P -wave reaching the i th AE probe, and v_p is the wave velocity of the P -wave. Note that x, y, z and t are all set manually.

The first-order Taylor expansion of arrival time is used to describe the arrival time t_{oi} of P wave detected by the corresponding i -probe, as shown below:

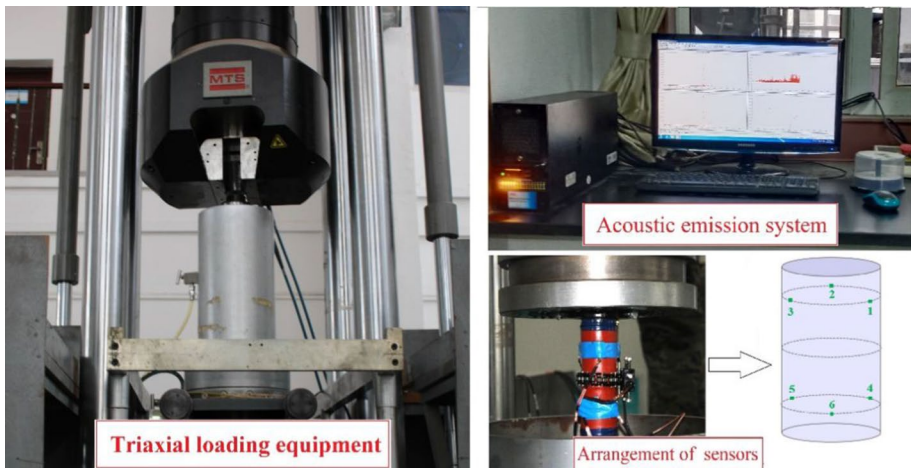


Fig. 3 The test system

$$t_{oi} = t_{ci} + \frac{\partial t_i}{\partial x} \Delta x + \frac{\partial t_i}{\partial y} \Delta y + \frac{\partial t_i}{\partial z} \Delta z + \frac{\partial t_i}{\partial t} \Delta t \tag{2}$$

where t_{ci} is the time when the P -wave reaches the i th probe calculated by the coordinates of the test point.

In formula (2), $\frac{\partial t_i}{\partial x}$, $\frac{\partial t_i}{\partial y}$, $\frac{\partial t_i}{\partial z}$ and $\frac{\partial t_i}{\partial t}$ can be expressed as:

$$\frac{\partial t_i}{\partial x} = \frac{(x_i - x)}{v_p R} \tag{3}$$

$$\frac{\partial t_i}{\partial y} = \frac{(y_i - y)}{v_p R} \tag{4}$$

$$\frac{\partial t_i}{\partial z} = \frac{(z_i - z)}{v_p R} \tag{5}$$

$$\frac{\partial t_i}{\partial t} = 1 \tag{6}$$

In formula (3–6), $R = \left[(x_i - x)^2 + (y_i - y)^2 + (z_i - z)^2 \right]^{\frac{1}{2}}$.

Based on formula (2), the value of probe number N determines the number of equations, that is, N probes correspond to N equations, which can be expressed as:

$$\mathbf{A} \Delta \boldsymbol{\theta} = \mathbf{B} \tag{7}$$

In the formula, the parameters are as follows:

$$\mathbf{A} = \begin{bmatrix} \frac{\partial t_1}{\partial x} & \frac{\partial t_1}{\partial y} & \frac{\partial t_1}{\partial z} & 1 \\ \frac{\partial t_2}{\partial x} & \frac{\partial t_2}{\partial y} & \frac{\partial t_2}{\partial z} & 1 \\ \vdots & \vdots & \vdots & \vdots \\ \frac{\partial t_n}{\partial x} & \frac{\partial t_n}{\partial y} & \frac{\partial t_n}{\partial z} & 1 \end{bmatrix}, \quad \Delta \boldsymbol{\theta} = \begin{bmatrix} \Delta x \\ \Delta y \\ \Delta z \\ \Delta t \end{bmatrix}, \quad \mathbf{B} = \begin{bmatrix} t_{o1} - t_{c1} \\ t_{o2} - t_{c2} \\ \vdots \\ t_{on} - t_{cn} \end{bmatrix} \tag{8}$$

The correction vector can be solved based on formula (7) with Gaussian elimination method, and the formulas are:

$$\mathbf{A}^T \mathbf{A} \Delta \boldsymbol{\theta} = \mathbf{A}^T \mathbf{B} \tag{9}$$

$$\mathbf{A}^T \mathbf{A} \Delta \boldsymbol{\theta} = (\mathbf{A}^T \mathbf{A})^{-1} \mathbf{A}^T \mathbf{B} \tag{10}$$

After obtaining the correction vector $\Delta \boldsymbol{\theta}$, using $\boldsymbol{\theta} + \Delta \boldsymbol{\theta}$ as a new test point, continuous iteration will be conducted until the error requirement between the new test point and the actual crack source location is met.

3 Triaxial compression failure characteristics of fractured granite

3.1 Stress–strain curve analysis

During the loading process, axial LVDT (Linear Variable Displacement Transducer) sensor and circumferential displacement sensor are used to monitor the deformation of the sample. Combined with the loading data, the full stress–strain curve of granite under 40 MPa confining pressure is obtained as shown in Fig. 4a–f. Under the condition of conventional triaxial compression, the stress–strain curves of intact and fractured granite are basically the same. At the initial stage of loading, the original micro-cracks and holes in the rock sample are compacted, and the stress–strain curve shows a certain concave trend. With the increase in axial pressure, the stress–strain curve increases linearly. At this time, the slope of axial strain is smaller than that of circumferential strain, and the rock produces more obvious compression deformation along the axial direction. Before rock failure, its structure deteriorates significantly, and the stress–strain curve becomes nonlinear. The stress after the peak value shows a more obvious drop characteristic, accompanied by a more brittle failure sound. At this time, the stress does not drop to zero and granite still has a certain compressive bearing capacity. The whole stress–strain curve includes compaction stage, elastic deformation stage, pre-peak failure stage and post-peak residual stage.

During the loading process of the intact rock sample, the internal stress of the rock mass is relatively uniform, and the stress–strain curve is relatively smooth. After the overall failure of the rock sample, the curve drops sharply, showing obvious brittle drop characteristics. The sample forms a single inclined plane shear failure. Compared with the intact rock sample, the existence of prefabricated fractures destroys the integrity of rock. For the fractured samples with 30°, 45° and 60° dip angles, the compaction characteristics of axial stress–strain curves are more obvious, and the compaction stage lasts longer than that of intact rock samples. In addition, during the failure process of the rock sample, multiple stress drops occur, and the stress fluctuation phenomenon is particularly obvious. At this time, the prefabricated fractures affect the stress characteristics of the rock. Under the load, stress concentration will occur at the fracture location, resulting in local damage. After the local failure of the rock, the load continues to be borne by other undamaged parts. When the applied load increases again, the position of stress concentration will be destroyed again, resulting in slip dislocation between the particles to form a new contact surface, and the stress will fluctuate synchronously and locally. It is repeated until the whole rock sample is destroyed, and every stress drop is actually the embodiment of crack propagation. Compared with the intact sample, the position of the shear crack formed by the fractured sample moves and the shape is more complex. Wing cracks, anti-wing cracks and coplanar cracks are generated around the fractures, and finally, the sample forms a through-cutting V-shape fracture surface failure or shear slip failure along the fracture surface. For 0° and 90° fractured rock samples, the sample forms a single inclined plane shear failure. The existence of fractures does not have a great influence on the rock failure mode. The macroscopic crack penetrates the fracture surface to form a single inclined plane shear failure. The corresponding stress–strain curve is similar to that of the intact sample. After reaching the peak strength, the curve decreases rapidly, and the curve shows obvious brittle drop characteristics.

Axial and circumferential stress–strain comparisons of granite are shown in Figs. 5 and 6. For fractured rock samples with 0° and 90° dip angles, the fracture destroys the integrity of the sample to a certain extent. With the axial loading, the axial strain slope of the

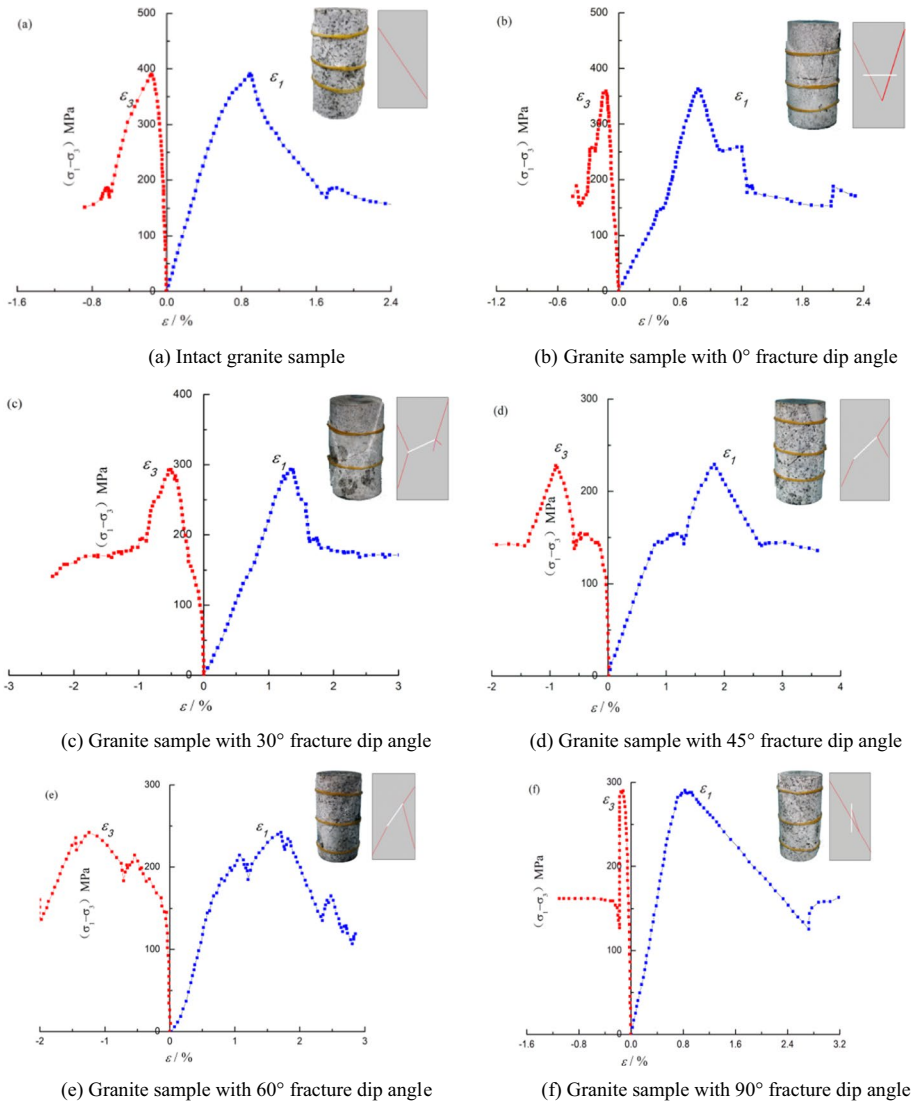


Fig. 4 Stress–strain curves under triaxial compressions. **a** Intact granite sample, **b** Granite sample with 0° fracture dip angle, **c** Granite sample with 30° fracture dip angle, **d** Granite sample with 45° fracture dip angle, **e** Granite sample with 60° fracture dip angle, and **f** Granite sample with 90° fracture dip angle

rock sample is smaller than that of the intact sample, but it is larger than that of 30°, 45° and 60° fractured granite, that is, the deformation resistance of 30°, 45° and 60° fractured samples < 0° and 90° fractured samples < intact samples. The circumferential deformation curves of intact rock samples and 0° and 90° fractured rock samples are similar. The circumferential strain slope of 30°, 45° and 60° fractured granite is smaller, that is, with the increase in axial load, the internal fractures of fractured rock samples develop gradually, resulting in more obvious lateral deformation.

3.2 Strength and deformation characteristics

Rock strength is an important factor of rock engineering stability (Feng et al. 2022; Wang et al. 2022; Song et al. 2022b). Figure 7 shows the comparison results of the average peak compressive strength of fractures with different dip angles. Compared with the peak strength of intact rock samples, the fractures destroy the structural integrity of the rock, causing the compressive strength to be less than 391.8 MPa of the intact samples, and the rock is more prone to fracture and instability. When the fracture dip angle increases from 0° to 45°, the average compressive strength of granite is 361.1, 302.3 and 222.2 MPa, respectively, showing a downward trend. When the fracture dip angle increases from 45° to 90°, the average compressive strength is 222.2, 234.3 and 290.3 MPa, respectively, showing an upward trend. With the increase of the fracture dip angle, the rock strength changes obviously, showing a nearly "U"-shaped changing trend of first decreasing and then increasing, and reaching the lowest strength value when the fracture dip angle is about 45°. In order to quantify the strength deterioration degree of fractured rock samples with different dip angles, the strength deterioration proportional coefficient k_1 is defined, as shown in formula (11). It is defined as the percentage of the strength difference between intact rock samples and fractured rock samples to the strength of intact rock samples.

$$k_1 = \frac{\sigma_c - \sigma_i}{\sigma_c} \times 100\% \tag{11}$$

In the formula, σ_c represents the strength value of the intact rock sample and σ_i represents the strength value of the fractured sample with i dip angle. Compared with the intact rock sample, the strength degradation proportional coefficient k_1 is 7.8~43.3%. The overall

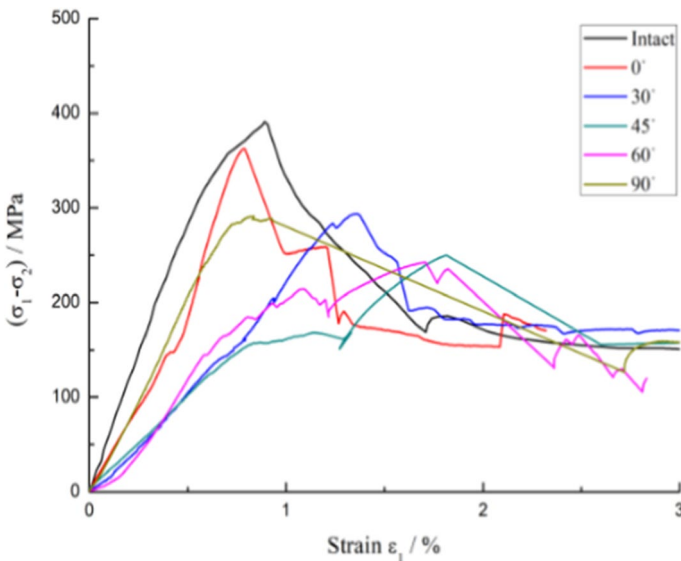


Fig. 5 Axial strain curves

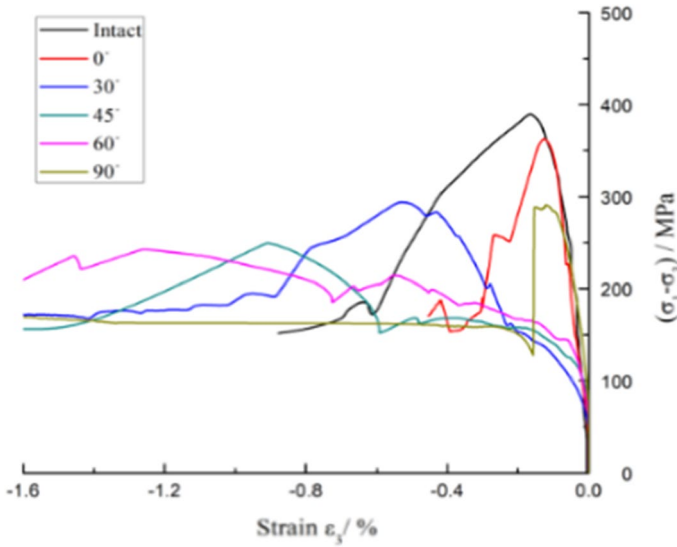


Fig. 6 Circumferential strain curves

bearing capacity decreases significantly, and the bearing capacity tends to be half when the fracture dip angle is 45°.

Figure 8 shows the curve of elastic modulus changing with the fracture dip angle. The existence of fractures increases the heterogeneity of rock samples and increases the slip interface inside the rock, so the slip amount in the axial compression process will also increase, resulting in the decrease in elastic modulus of rock samples. Formula (12) defines the deterioration proportional coefficient k_2 of elastic modulus, that is, percentage of elastic modulus difference between intact rock sample and fractured rock sample to the elastic modulus of intact rock samples.

$$k_2 = \frac{E_c - E_i}{E_c} \times 100\% \tag{12}$$

In the formula, E_c represents the elastic modulus of the intact rock sample and E_i represents the elastic modulus of the fractured sample with i dip angle. For the fractured rock samples with 0° and 90° dip angles, the elastic modulus is 47.6 and 45.1 GPa, respectively. Compared with the 51.5 GPa of the intact sample, the deterioration proportional coefficients k_2 of elastic modulus are 7.5 and 12.4%, respectively, and the deterioration degree is relatively small. For the fractured rock samples with 30°, 45° and 60° dip angles, the degradation proportional coefficients k_2 are as high as 48.0, 66.9 and 49.6%, respectively. Especially, when the dip angle is 45°, the degradation of deformation characteristics is the most obvious. The variation law of elastic modulus of fractured rock samples with dip angle is: $E_{\text{intact}} > (E_{0^\circ}, E_{90^\circ}) > (E_{30^\circ}, E_{60^\circ}) > E_{45^\circ}$, showing a nearly U-shaped changing trend of first decreasing and then increasing. The specific results are shown in Table 2.

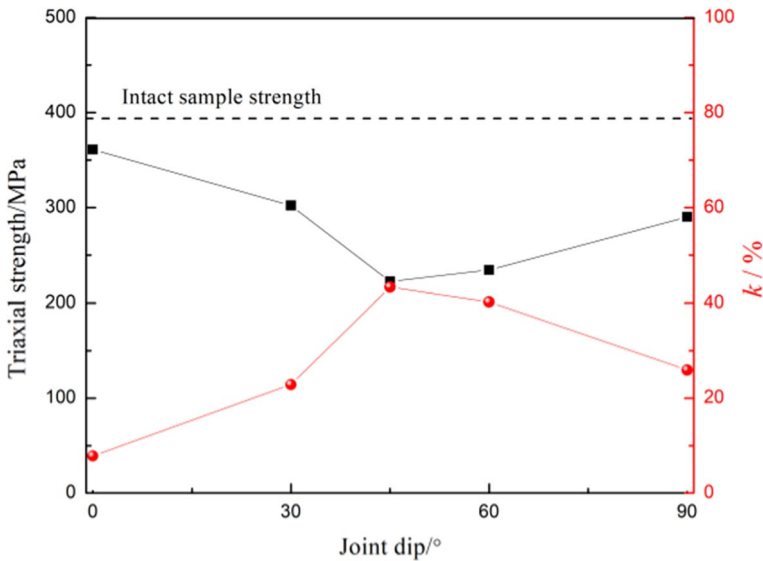


Fig. 7 Evolution of triaxial compressive strength with fracture dip angle (A1 ~ F1)

4 Acoustic emission characteristics

In the fracture process of rock, part of the elastic strain energy stored in the rock mass will release acoustic emission signals in the form of elastic waves. Therefore, the use of acoustic emission time–space distribution, ring count, energy and other parameters is an effective method to analyze and determine the degree of rock internal fracture and fracture evolution process (Niu et al. 2021; Schweidler et al. 2022).

4.1 Three-dimensional space–time evolution characteristics of acoustic emission

The three-dimensional time–space evolution results of acoustic emission can directly reflect the initial position of the internal fracture event of rock, the damage status of rock and the development degree of fractures at different loading stages, which lays a foundation for in-depth research on the crack growth process and spatial morphology (Chu et al. 2020; Niu et al. 2020). Figure 9 shows the results of acoustic emission three-dimensional positioning of granite samples with different dip angles under triaxial loading, including pore fracture compaction stage I at the initial stage of loading, linear elastic deformation stage II, unstable fracture development stage III, and post-peak fracture stage IV. Three-dimensional display is conducted according to the amplitude and occurrence time of acoustic emission source. The amplitude (unit: dB) of acoustic emission source is distinguished by the size and color of the ball. The larger the amplitude of acoustic emission source is, the larger the size of the ball is, and the deeper the color is, and vice versa.

It can be seen from Fig. 9 that in the initial stage of loading (stage I), the primary fractures in the rock sample are closed, and a small number of randomly distributed events occur. The frequency and intensity are low, and the amplitude intensity is below 60 dB.

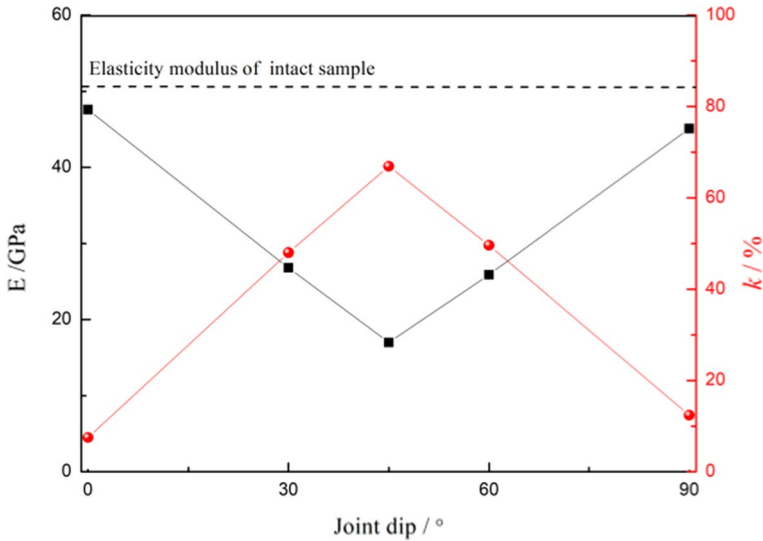


Fig. 8 Evolution of elastic modulus with fracture dip angle (A1 ~F1)

That is, at this stage, the damage of granite sample is very small, and there is almost no crack initiation or propagation activity inside. With the increase in external load, the rock sample enters the linear elastic deformation stage II. At this time, the external driving energy is mainly converted into the elastic strain energy of granite sample, the acoustic emission event growth is not obvious, and the overall damage degree of rock is small. When the loading process enters stage III, the acoustic emission event enters an active stage, indicating that the development of micro-cracks has undergone a qualitative change. At this stage, the number of acoustic emission event points increases dramatically, and the number of fracture events with amplitude intensity between 80 and 100 dB increases significantly. The internal fractures of the rock continue to initiate, propagation, and coalescence and produce large fracture events, resulting in the sample entering a subcritical instability state. When the driving load is further increased, the nucleation area of the acoustic emission event points converges and forms, and the rock damage increases sharply, forming a macro-failure zone. The sample changes from subcritical instability to failure instability. At this time, the number of event points corresponding to intact granite samples and granite samples with various fracture dip angles is 5359, 5440, 1314, 671, 3739 and 4820, respectively, showing a variation law of first decreasing and then increasing. For fractured rock samples with 0° and 90° dip angles, the number of fracture events is similar to that of intact rock samples, and a large range of failure areas are formed. For other dip angle samples, the acoustic emission fractures are distributed around the initial cracks and expand to form through cracks, with a more concentrated event distribution. In addition, the acoustic emission signal intensity of the fractured granite sample decreases significantly, indicating that the degree of the rock fracture activity decreases significantly. At this time, the acoustic emission signal strength E presents the following rule: $E_{\text{intact}} > (E_{0^\circ}, E_{90^\circ}) > (E_{30^\circ}, E_{60^\circ}) > E_{45^\circ}$. The overall change is nearly "U" shaped, and the severity of damage decreases first and then increases.

Table 2 Test results of triaxial compression experiment

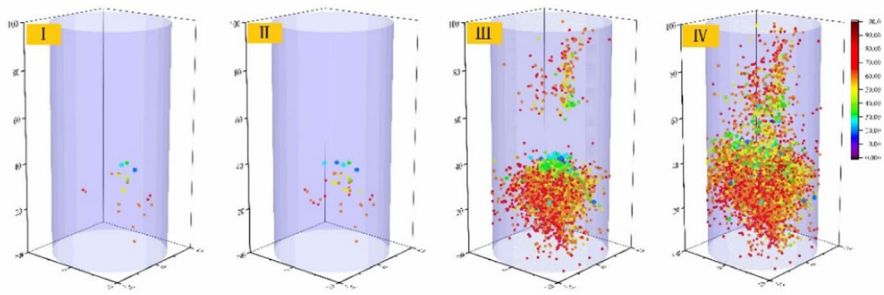
θ /°	Serial number	Triaxial compression strength/MPa	Average strength/MPa	k_1 /%	E /GPa	Average E /GPa	k_2 /%
Intact sample	A1	391.9	391.8	–	53.0	51.5	–
	A2	386.5			50.2		
	A3	397.0			51.2		
0	B1	362.4	361.1	7.8	49.9	47.6	7.5
	B2	356.5			45.6		
	B3	364.3			47.3		
30	C1	293.8	302.3	22.9	24.4	26.8	48.0
	C2	302.8			26.3		
	C3	310.2			29.6		
45	D1	229.8	222.2	43.3	16.2	17.0	66.9
	D2	209.3			18.3		
	D3	227.6			16.6		
60	E1	242.7	234.3	40.2	27.7	25.9	49.6
	E2	235.5			25.2		
	E3	224.6			24.9		
90	F1	291	290.3	25.91	43	45.1	12.4
	F2	281.8			48		
	F3	298			44.2		

k_1 is strength degradation proportional coefficient, and k_2 is elastic modulus degradation proportional coefficient

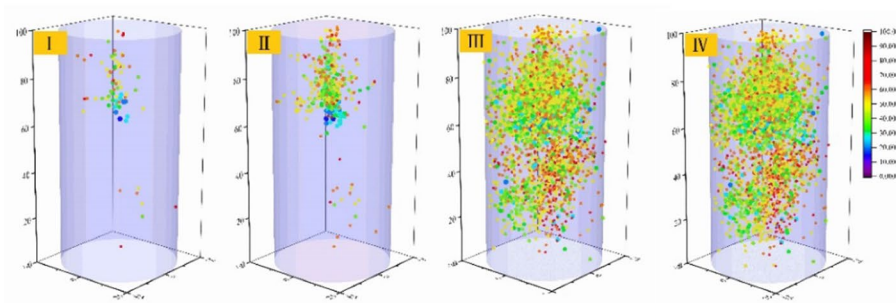
4.2 Acoustic emission ringing evolution law

Acoustic emission ringing characteristics can reflect the activity of rock internal fracture events and the damage degree of rock (Andrew et al. 2015; Barão et al. 2021; Zha et al. 2021; Dinmohammadpour et al. 2022), so it is widely used to describe and evaluate the fracture characteristics of materials.

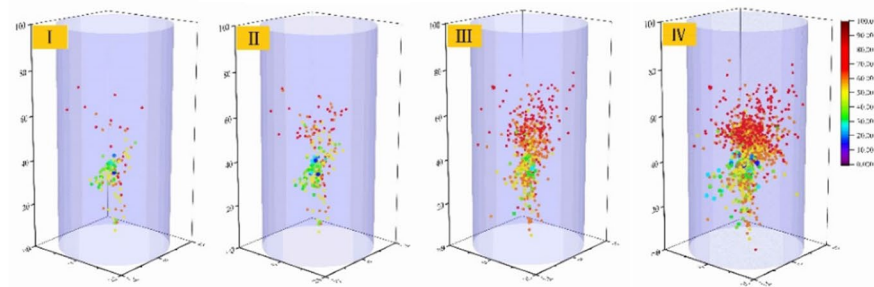
Under different fracture characteristics, the variation law of ring count is relatively consistent (as shown in Fig. 10). At the initial stage of loading, the primary fractures inside the rock sample are closed, and sporadic acoustic emission phenomena occur. Its frequency and intensity are very small, and the ring count is generally below 2.0×10^3 times, indicating that there is little damage to the granite sample in this stage, and there is almost no crack initiation or propagation activity in the inside. The cumulative ring count is maintained at a low level, and the acoustic emission activity of the rock sample is in a quiet period. Subsequently, the rock sample enters the elastic–plastic stage. In the first part of this stage, the internal cracks of the sample are constantly initiated and expanded, and the acoustic emission ringing rate shows a slow and irregular fluctuation growth. However, its growth amplitude is small, and the values are not greater than 10×10^3 times. The cumulative ring count of the sample enters a slow rising period. With the further increase of the load, the sample enters the late stage of the elastic–plastic stage, and the sample reaches the critical instability state. The fractures in the rock gradually migrate and propagate in an aggregated manner, and the damage increases sharply, leading to a sudden increase in the



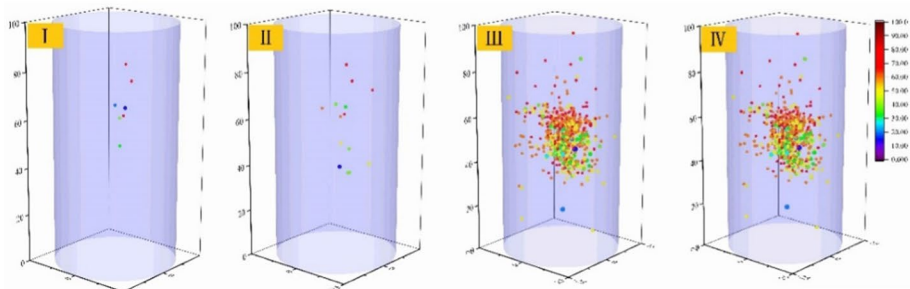
(a) Intact granite sample



(b) Granite sample with 0° fracture dip angle



(c) Granite sample with 30° fracture dip angle



(d) Granite sample with 45° fracture dip angle

Fig. 9 Three-dimensional space–time evolution process of acoustic emission events. **a** Intact granite sample, **b** Granite sample with 0° fracture dip angle, **c** Granite sample with 30° fracture dip angle, **d** Granite sample with 45° fracture dip angle, **e** Granite sample with 60° fracture dip angle, and **f** Granite sample with 90° fracture dip angle

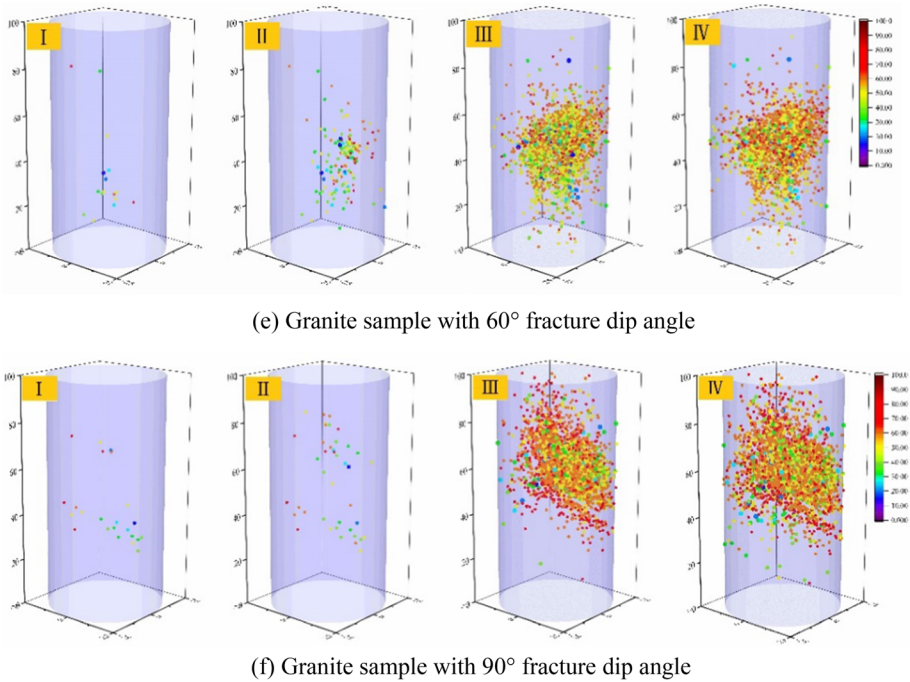


Fig. 9 (continued)

cumulative ring count. The acoustic emission activity enters the active period. Compared with the early stage of the elastic–plastic stage, the growth of AE ring count rate shows an order of magnitude difference. The count rate turns to a rapid growth stage, and the peak value of the ring rate appears at a certain time point. It indicates that the internal cracks of the rock propagate and coalesce rapidly, large fractures of the rock sample appear, and the cumulative ring count enters a rapid growth period. At this time, it can be observed that the ring count rate before and after the peak point has obvious fluctuation characteristics. This is because the crack tip is in the dynamic cyclic process of stress concentration → crack growth → stress release after the sample enters the unstable propagation stage, so the crack growth shows a "phase step" growth characteristic (Feng et al. 2022). In addition, the time when the AE ring count rate reaches the peak lags slightly behind the time when the stress peak value occurs. It indicates that the granite sample has been destroyed completely after the peak stress suddenly decreases and macro-cracks appear. With the increase in axial displacement, friction slip occurs on the section of the sample and the loading curve enters the residual strength stage. The AE ring count rate decreases sharply and the acoustic emission events of some rock samples even disappear. In this process, only a few cracks are generated on the sample. The characteristics of quiet, active and dramatic changes of the acoustic emission ringing well reflect the damage evolution process inside the rock sample.

The existence of fractures destroys the integrity of rock. Compared with intact rock samples, fractured rock samples do not break at one time during the loading process. Fractured rock samples have multiple stress drops during the failure process, and the acoustic emission ring count rate increases sharply each time the stress drop occurs.

The different angles of the prefabricated cracks lead to the change of the stress mode of the sample. It changes the history of crack development during the failure process of

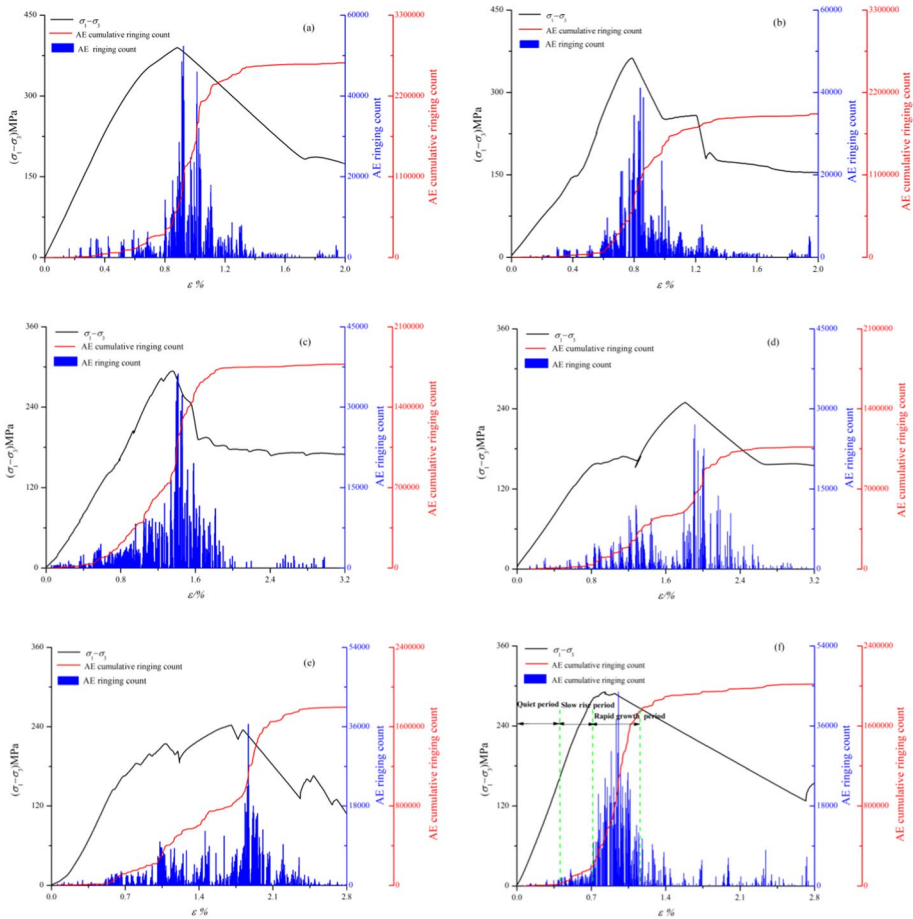


Fig. 10 AE ring count curves of granite specimens under triaxial compression: **a** Intact specimen; **b** $v = 0^\circ$; **c** $v = 30^\circ$; **d** $v = 45^\circ$; **e** $v = 60^\circ$; **f** $v = 90^\circ$

the sample, thus leading to the different changing trends of the ring count (Fig. 11). For fractured rock samples with dip angles of 0° and 90° , the growth characteristics are similar to those of intact rock samples in the process of loading failure, and the slow rising period of ringing is relatively short, so the crack development is not sufficient. When the fracture enters the stage of rapid propagation, the ring count increases sharply, with a strong concentration and a strong activity. The number of peak ring counts is 4.11×10^4 times and 4.36×10^4 times, respectively, and the rock has severe sudden instability when the strains are 0.84% and 1.09%. For fractured rock samples with dip angles of 30° , 45° and 60° , the slow rise period of the ringing is long, and the rock fractures have obvious progressive expansion stage. At this time, the fully developed fractures have a greater cumulative damage to the rock. When the driving stress reaches the peak value, the crack growth enters the rapid expansion stage. The slip dislocation occurs between the rock particles and a new contact surface is formed, which eventually leads to the loss of bearing capacity of the rock sample and the overall failure. Relatively speaking, the number of peak ring counts is small, which is 3.62×10^4 times, 3.1×10^4 times and 3.66×10^4 times, respectively, and

the corresponding strains are 1.41%, 1.91% and 1.86%, respectively. The acoustic emission signal shows obvious 'migration' phenomenon, and the large-scale fracture events will occur after the rock sample is subjected to greater load. Furthermore, it can be found that with the dip angles increasing from 0° to 90°, the peak values of acoustic emission ring count rate are 4.11×10^4 , 3.62×10^4 , 3.1×10^4 , 3.66×10^4 and 4.36×10^4 , respectively, and the peak values of acoustic emission ring count rate first decrease and then increase. In fact, this is closely related to the mode of "through-cutting fracture surface failure" and "sliding failure along fracture surface" in Sect. 3.1. The different failure modes change the course of crack development in the process of sample failure and affect the course of crack initiation, propagation, nucleation and penetration failure, resulting in the difference of ring count characteristics.

4.3 Acoustic emission energy characteristics

The acoustic emission energy can reflect the elastic energy released by the sample during the failure process due to crack propagation. The energy of a single acoustic emission signal is defined as follows (Lin et al. 2018; Bruning et al. 2018; Zhang et al. 2018; Mastrogiannis et al. 2019).

$$E = \frac{1}{R} \int_{t_i}^{t_j} U^2(t)dt \tag{13}$$

In the formula, t_i is the time when the acoustic emission event signal exceeds the threshold voltage for the first time and t_j is the time when it falls to the threshold voltage again. The R is the internal resistance value of acoustic emission instrument. The energy result calculated by Formula (3) is the absolute energy value of acoustic emission, which is closely related to the impact number and amplitude of acoustic emission. It can better reflect the relative energy or intensity of the fracture event, so it is often used to reflect the acoustic emission activity.

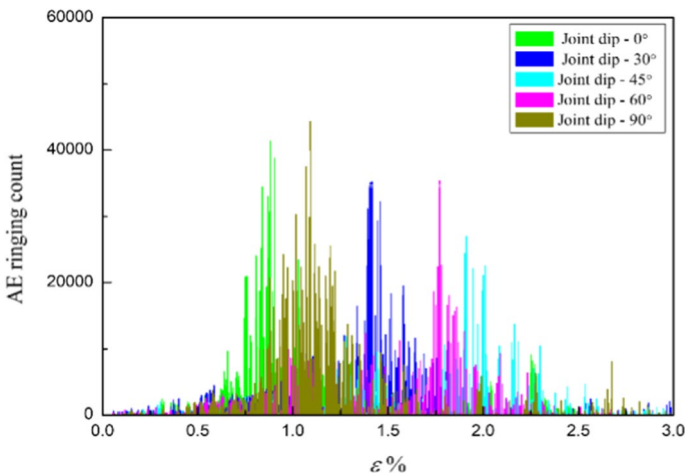


Fig. 11 AE ring count rate of rock specimens under triaxial compression

The evolution law of rock loading acoustic emission energy is relatively consistent. Taking Fig. 12 as an example, in the early stage of loading, the energy rate is generally between 0 and 1000 mV*mS, its magnitude is at a low level, and its cumulative energy approximately shows a linear low-speed growth. At this time, the rock is in the pore/fissure compression stage and elastic deformation stage, and the initiation and propagation of internal cracks in granite are relatively small. With the loading process, the release of stress and the dissipation of energy lead to the fracture of different parts of the rock. There is a small sudden increase in energy, and several high energy points appear before the peak. For example, at the strains of 0.427% and 0.494%, the acoustic emission energy values are 10,000 and 17,777 mV*mS, respectively. The small sudden increase in acoustic emission energy indicates that the adjustment, concentration and release of stress, as well as the accumulation, dissipation and release of energy also change accordingly. When the strain reaches 0.861%, the peak value of acoustic emission energy is 78,778 mV*mS, and the energy value has an order of magnitude change. At this time, due to the continuous accumulation of energy in the process of deformation and failure of the rock sample, a large amount of elastic energy is suddenly released when macroscopic through cracks are generated, and the accumulated energy curve synchronously enters a rapid growth stage.

Compared with intact sample, the fracture affects the energy release process of the rock to a certain extent. Before the internal energy forms the main fracture, the fracture events with large energy increase significantly, and the curve of energy accumulation number changing with time shows a phase step growth. In addition, the fracture destroys the integrity of the rock to a certain extent. When the macro-fracture is formed, the corresponding energy rate is generally lower than that of the intact sample, and the intensity at the moment of failure decreases obviously. For rock samples with different fracture dip angles, there are some differences in the evolution law of acoustic emission energy (Fig. 13). As the dip angles increase from 0° to 90°, the instantaneous elastic strain energy released when the rock changes from subcritical stable state to fracture unstable state is 78778, 70,017, 52,361, 63,880 and 72,576 (mV*mS), which is far less than 90,997 mV*mS of the intact sample. The elastic strain energy shows a changing trend of first decreasing and then increasing, and the energy rate of rock sample with 45° dip angle is the minimum.

5 Conclusion

In this paper, the conventional triaxial compression test of prefabricated fractured granite is conducted, the deformation, strength and acoustic emission characteristics of rocks with different dip angles are analyzed, and the damage and failure mechanism of rocks is explored. The main conclusions are as follows:

- (1) The characteristics of rock stress–strain curve are significantly affected by fractures. In the process of failure, the local stress fluctuation of the fractured rock sample is obvious and the stress drop occurs for many times. Especially for the fractured samples with 30°, 45° and 60° dip angles, the brittle characteristics are weakened and the plastic characteristics are enhanced.
- (2) Due to the difference of fracture dip angles, the failure of granite sample shows two modes: "through-cutting fracture surface failure" and "shear failure along fracture surface." For fractures with 0° and 90° dip angles, there is no significant influence on

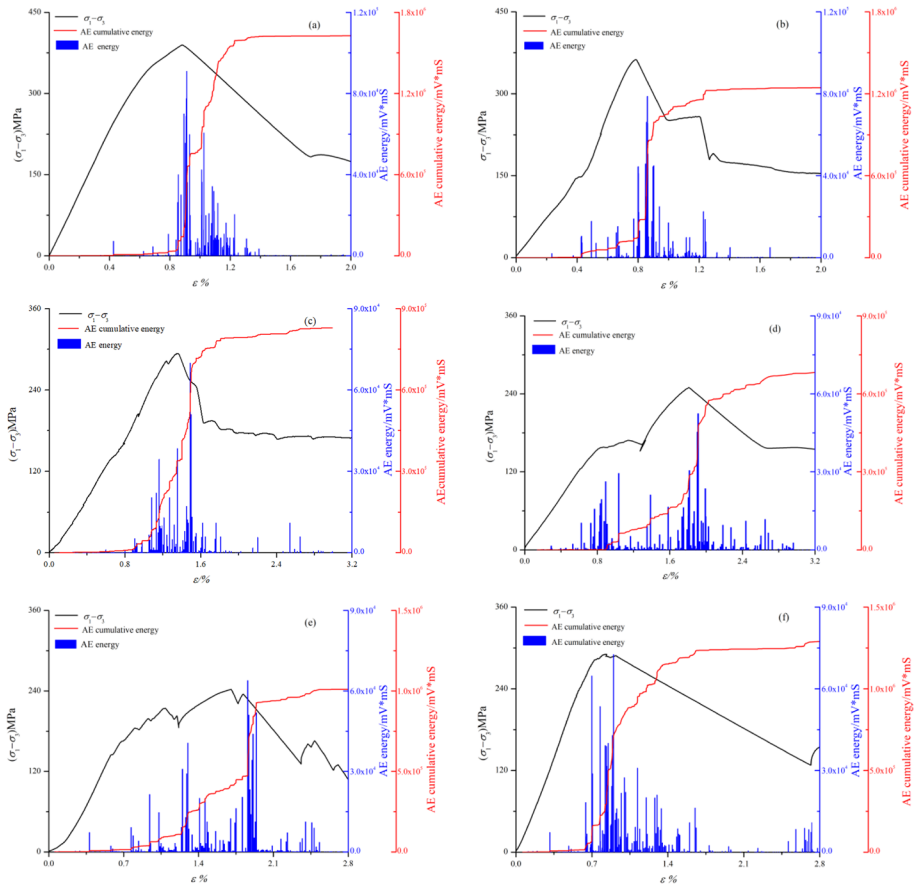


Fig. 12 AE energy curves of granite samples under triaxial compression: **a** Intact specimen; **b** $\nu=0^\circ$; **c** $\nu=30^\circ$; **d** $\nu=45^\circ$; **e** $\nu=60^\circ$; **f** $\nu=90^\circ$

the failure mode of rock, and the macro-fractures cut through the fracture surface to form single inclined shear failure or "U" type failure. For fractured rock samples with 30° , 45° and 60° dip angles, wing cracks, anti-wing cracks and coplanar cracks are generated around the fractures, and finally, the samples form shear slip failure along the fracture surface.

- (3) The fractures destroy the structural integrity of rock, resulting in the reduction of rock resistance to load and deformation. With the increase in fracture dip angles from 0° to 90° , the compressive strength and elastic modulus of rock samples show a nearly "U"-shaped changing trend of decreasing first and then increasing, and the deterioration ratio coefficients are 7.8 ~ 43.3% and 7.5 ~ 66.9%, respectively.
- (4) The fracture dip angle affects the variation law of AE signals during the fracture process. Especially for the fractured rock samples with 30° , 45° and 60° dip angles, the AE ring count and energy show obvious "migration" phenomenon, and the signal concentration distribution area is widened and moved backward. With the increase in dip angle, the active degree of rock fracture decreases at first and then increases.

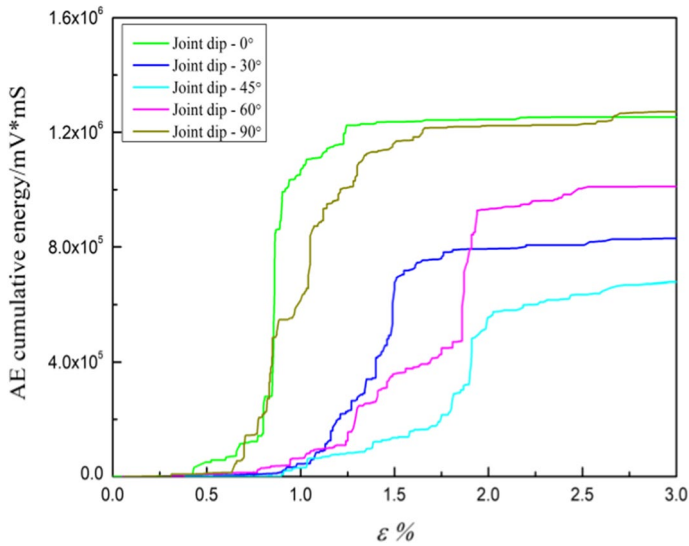


Fig. 13 Acoustic emission cumulative energy curve

Funding The authors sincerely thank the financial support from the National Natural Science Foundation of China (No. 42002275), the National Natural Science Foundation of Zhejiang province (No. LQ21D020001), the Collaborative Innovation Center for Prevention and Control of Mountain Geological Hazards of Zhejiang Province (No. PCMGH-2021-03), the Shaoxing Science and Technology Plan Project (No. 2022A13003).

Declarations

Conflict of interest The authors have not disclosed any competing interests.

References

- Andrew J, Ramesh C (2015) Residual strength and damage characterization of unidirectional glass–basalt hybrid/epoxy CAI laminates. *Arab J Sci Eng* 40(6):1695–1705. <https://doi.org/10.1007/s13369-015-1651-8>
- Barão VA, Ramachandran RA, Matos AO, Badhe RV, Grandini CR, Sukotjo C, Mathew M (2021) Prediction of tribocorrosion processes in titanium-based dental implants using acoustic emission technique: Initial outcome. *Mater Sci Eng* 123:112000. <https://doi.org/10.1016/j.msec.2021.112000>
- Bruning T, Karakus M, Nguyen GD, Goodchild D (2018) Experimental study on the damage evolution of brittle rock under triaxial confinement with full circumferential strain control. *Rock Mech Rock Eng* 51(11):3321–3341. <https://doi.org/10.1007/s00603-018-1537-7>
- Chu CQ, Wu SC, Zhang SH, Guo P, Zhang M (2020) Mechanical behavior anisotropy and fracture characteristics of bedded sandstone. *J Cent South Univ* 51(8):2232–2246. <https://doi.org/10.11817/j.issn.1672-7207.2020.08.018>
- Dinmohammadpour M, Nikkhah M, Goshtasbi K, Ahangari K (2022) Application of wavelet transform in evaluating the Kaiser effect of rocks in acoustic emission test. *Measurement* 192:110887. <https://doi.org/10.1016/j.measurement.2022.110887>
- Duan G, Li J, Zhang J, Luo Z, Wan L, Li B (2019) The mechanical behaviour of rock specimens with specific edge crack distributions under triaxial loading conditions. *J Geophys Eng* 16(5):962–973. <https://doi.org/10.1093/jge/gxz059>

- Feng Q, Jin J, Zhang S, Liu W, Yang X, Li W (2022) Study on a damage model and uniaxial compression simulation method of frozen–thawed rock. *Rock Mech Rock Eng* 55(1):187–211. <https://doi.org/10.1007/s00603-021-02645-2>
- Huang YH, Yang SQ, Ju Y, Zhou XP, Gao F (2016) Experimental study on mechanical behavior of rock-like materials containing pre-existing intermittent fissures under triaxial compression. *Chin J Geotech Eng* 38(7):1212–1220. <https://doi.org/10.11779/CJGE201607007>
- Huang K, Lin P, Tang C, Zhou J (2002) Study on the coalescence mechanism of intermittent preset cracks under biaxial loading. *Chin J Rock Mech Eng* 21(6):808–816. <https://doi.org/10.3321/j.issn:1000-6915.2002.06.010>
- Latyshhev OG, Prishchepa DV (2020) Fractured rock mass modeling and stress–strain analysis using the finite element method. *Gornyi Zhurnal* 5:11–14. <https://doi.org/10.17580/gzh.2020.05.01>
- Lee H, Jeon S (2011) An experimental and numerical study of fracture coalescence in pre-cracked specimens under uniaxial compression. *Int J Rock Mech Min* 48(6):979–999. <https://doi.org/10.1016/j.ijsostr.2010.12.001>
- Li D, Wang C, Xue D, Yi H, Zhong J (2015) Numerical simulation on compressive strength of single jointed rock mass. *J Liaoning Tech Univ* 34(02):150–154. <https://doi.org/10.11956/j.issn.1008-0562.2015.02.002>
- Lin Q, Mao D, Wang S, Li S (2018) The influences of mode II loading on fracture process in rock using acoustic emission energy. *Eng Fract Mech* 194:136–144. <https://doi.org/10.1016/j.engfracmech.2018.03.001>
- Liu T, Li X, Zheng Y, Meng F, Song D (2020) Analysis of seismic waves propagating through an in situ stressed rock mass using a nonlinear model. *Int J Geomech* 20(3):04020002. [https://doi.org/10.1061/\(ASCE\)GM.1943-5622.0001621](https://doi.org/10.1061/(ASCE)GM.1943-5622.0001621)
- Li YP, Chen LZ, Wang YH (2005) Experimental research on pre-cracked marble under compression. *Int J Solids Struct* 42(10):2505–2516. <https://doi.org/10.1016/j.ijsostr.2004.09.033>
- Luo Y, Gong H, Huang J, Wang G, Li X, Wan S (2022) Dynamic cumulative damage characteristics of deep-buried granite from Shuangjiangkou hydropower station under true triaxial constraint. *Int J Impact Eng* 165:104215. <https://doi.org/10.1016/j.ijimpeng.2022.104215>
- Mastrogiannis D, Andreopoulos SI, Potirakis SM (2019) A comparative study by using two different log-periodic power laws on acoustic emission signals from LiF specimens under compression. *Eng Fract Mech* 210:170–180. <https://doi.org/10.1016/j.engfracmech.2018.04.022>
- Mohammadi H, Pietruszczak S (2019) Description of damage process in fractured rocks. *Int J Rock Mech Min* 113:295–302. <https://doi.org/10.1016/j.ijrmms.2018.12.003>
- Niu Y, Zhou XP (2021) Forecast of time-of-instability in rocks under complex stress conditions using spatial precursory AE response rate. *Int J Rock Mech Min Sci* 147:104908. <https://doi.org/10.1016/j.ijrmms.2021.104908>
- Niu Y, Zhou XP, Berto F (2020) Temporal dominant frequency evolution characteristics during the fracture process of flawed red sandstone. *Theor Appl Fract Mech* 110:102838. <https://doi.org/10.1016/j.tafmec.2020.102838>
- Niu Y, Hu Y, Wang JG (2023) Cracking characteristics and damage assessment of filled rocks using acoustic emission technology. *Int J Geomech*. <https://doi.org/10.1061/IJGNAI.GMENG-8034>
- Rudziński Ł, Mirek K, Mirek J (2019) Rapid ground deformation corresponding to a mining-induced seismic event followed by a massive collapse. *Nat Hazards* 96(1):461–471. <https://doi.org/10.1007/s11069-018-3552-0>
- Schweidler S, Dreyer SL, Breitung B, Brezesinski T (2022) Acoustic emission monitoring of high-entropy oxyfluoride rock-salt cathodes during battery operation. *Coatings* 12(3):402. <https://doi.org/10.3390/coatings12030402>
- Shahbazi A, Chesnaux R, Saeidi A (2021) A new combined analytical-numerical method for evaluating the inflow rate into a tunnel excavated in a fractured rock mass. *Eng Geol* 283:106003. <https://doi.org/10.1016/j.enggeo.2021.106003>
- Song L, Jiang Q, Zhong Z, Dai F, Wang G, Wang X, Zhang D (2022) Technical path of model reconstruction and shear wear analysis for natural joint based on 3D scanning technology. *Measurement* 188:110584. <https://doi.org/10.1016/j.measurement.2021.110584>
- Song L, Wang G, Wang X, Huang M, Xu K, Han G, Liu G (2022b) The influence of joint inclination and opening width on fracture characteristics of granite under triaxial compression. *Int J Geomech* 22(5):04022031. [https://doi.org/10.1061/\(ASCE\)GM.1943-5622.0002372](https://doi.org/10.1061/(ASCE)GM.1943-5622.0002372)
- Wang G, Song L, Liu X, Bao C, Lin MQ, Liu GJ (2022) Shear fracture mechanical properties and acoustic emission characteristics of discontinuous jointed granite. *Rock Soil Mech* 43(06):1533–1545
- Yang S, Wen S, Li L (2007) Experimental study on deformation and strength properties of coarse grained marbles with discontinuous pre-existing cracks under different confining pressures. *Chin J Rock Mech Eng* 8:1572–1587. <https://doi.org/10.3321/j.issn:1000-6915.2007.08.007>
- Yu H, Liu SW, Jia HS (2020) Mechanical response and energy dissipation mechanism of closed single fractured sandstone under different confining pressures. *J Min Saf Eng* 37:385–393. <https://doi.org/10.13545/j.cnki.jmse.2020.02.019>

- Zha E, Zhang Z, Zhang R, Wu S, Zhou J (2021) Long-term mechanical and acoustic emission characteristics of creep in deeply buried jinping marble considering excavation disturbance. *Int J Rock Mech Min* 139(2):104603. <https://doi.org/10.1016/j.ijrmms.2020.104603>
- Zhang M, Liu S, Shimada H (2018) Regional hazard prediction of rock bursts using microseismic energy attenuation tomography in deep mining. *Nat Hazards* 93(3):1359–1378. <https://doi.org/10.1007/s11069-018-3355-3>
- Zhao XD, Liu JP, Li YH, Tian J, Zhu WC (2008) Experimental verification of rock locating technique with acoustic emission. *Chin J Geotech Eng* 30(10):1472–1476
- Zuo SY, Ye ML, Tan XL (2013) Numerical model and validation of failure mode for underground caverns in layered rock mass. *Rock Soil Mech* 34(1):458–465. <https://doi.org/10.16285/j.rsm.2013.s1.020>

Publisher's Note Springer Nature remains neutral with regard to jurisdictional claims in published maps and institutional affiliations.

Springer Nature or its licensor (e.g. a society or other partner) holds exclusive rights to this article under a publishing agreement with the author(s) or other rightsholder(s); author self-archiving of the accepted manuscript version of this article is solely governed by the terms of such publishing agreement and applicable law.